



Cite this: *Phys. Chem. Chem. Phys.*, 2024, 26, 6752

# Dynamical effects on the $O(^3P) + D_2$ reaction and its impact on the $\Lambda$ -doublet population

A. Veselinova,<sup>a</sup> M. Menéndez,<sup>b</sup> L. González-Sánchez,<sup>a</sup> A. Zanchet,<sup>c</sup> F. J. Aoiz<sup>b</sup> and P. G. Jambrina<sup>\*a</sup>

The  $O(^3P) + D_2 \rightarrow OD(^2\Pi) + D$  reaction presents the peculiarity of taking place on two different potential energy surfaces (PESs) of different symmetry,  $^3A'$  and  $^3A''$ , which become degenerate for collinear configurations where the saddle-point of the reaction is located. The degeneracy is broken for non-collinear approaches with the energy on the  $^3A'$  PES rising more abruptly with the bending angle, making the frequency of this mode higher on the  $^3A'$  state. Consequently, the  $^3A'$  PES should be less reactive than the  $^3A''$  one. Nevertheless, quantum scattering calculations show that the cross section is higher on the  $^3A'$  PES for energies close to the classical reaction threshold and rotationless reactant. It is found that the differences between the reactivity on the two PESs are greater for low values of total angular momentum, where the centrifugal barrier is lower and contribute to the higher population of the  $\Pi(A')$   $\Lambda$ -doublet states of OD at low collision energies. At high collision energies, the  $\Pi(A')$   $\Lambda$ -doublet state is also preferentially populated. Analysis of the differential cross sections reveals that the preponderance for the  $\Pi(A')$   $\Lambda$ -doublet at low energies comes from backward scattering, originating from the reaction on the  $^3A'$  PES, while at high energies, it proceeds from a different mechanism that leads to sideways scattering on the  $^3A''$  PES and that populates the  $\Pi(A')$  manifold.

Received 13th November 2023,  
Accepted 17th January 2024

DOI: 10.1039/d3cp05510h

rsc.li/pccp

## 1 Introduction

The dynamics of the gas-phase reaction between atomic oxygen and molecular hydrogen has been widely studied experimentally<sup>1–4</sup> and computationally<sup>5–18</sup> due to its importance in combustion processes, the chemistry of the upper atmosphere, and the chemistry of the OH radical in the interstellar space. In combustion, it is important for chain branching and propagation during the combustion of hydrogen and hydrocarbons.<sup>19,20</sup> In spite of being associated with a high activation barrier ( $\sim 0.6$  eV),<sup>7,17</sup> it is also one of the most important sources of OH in the mesosphere, where collisions between atomic oxygen and vibrationally excited  $H_2$  account for 4–19% of the OH produced.<sup>21</sup> This reaction is also one of the major sources of OH in several astronomical environments,<sup>22–28</sup> in particular in the photon-dominated regions and protoplanetary disks where  $H_2$  can be efficiently pumped to excited vibrational states. It is also one of the benchmark systems for kinetics, and their thermal rate coefficients have been measured using different techniques in a wide range of temperatures (see ref. 29 for a

compilation). For the particular case of the reaction between  $O(^3P)$  and  $D_2$ , experimental rate coefficients have been obtained in ref. 30–34.

The mechanism of the  $O(^3P) + H_2 \rightarrow OH(^2\Pi) + H$  reaction can be described as the simultaneous homolytic cleavage of the H–H bond and formation of a new O–H bond. The oxygen atom has four electrons distributed in three p orbitals ( $p^4$ ), such that in its electronic ground state it has two single and one double occupied valence p orbitals. At the reactant asymptote, before O and  $H_2$  begin to interact, there are three degenerate potential energy surfaces (PESs), one PES of  $^3A'$  symmetry (where the two p single occupied orbitals of the oxygen atom lie on the three-atom plane), and two PESs of  $^3A''$  symmetry (in which one of the two singly occupied p orbitals is perpendicular to the three-atom plane). The formation of the O–H bond is only possible if one of the oxygen's singly occupied p orbitals points towards  $H_2$ ,<sup>35</sup> which occurs on the  $^3A'$  and one of the  $^3A''$  PESs, which are degenerate for collinear approaches, resulting from the  $\Pi$  character of the linear arrangement. The second  $^3A''$  PES represents the situation in which the doubly occupied p orbital points towards  $H_2$  and is therefore repulsive and cannot give rise to the reaction. At the product asymptote, the open-shell  $OH(^2\Pi)$  molecule is formed, for which the rotational levels split into two spin-orbit states, and each of them splits into a pair of  $\Lambda$ -doublet levels.  $\Lambda$ -doublet states can be labelled as  $\Pi(A')$  or  $\Pi(A'')$  where the symmetry index indicates the location of the

<sup>a</sup> Departamento de Química-Física, Universidad de Salamanca, Salamanca, 37008, Spain. E-mail: [pjambrina@usal.es](mailto:pjambrina@usal.es)

<sup>b</sup> Departamento de Química-Física, Universidad Complutense de Madrid, Madrid, 28040, Spain

<sup>c</sup> Instituto de Física Fundamental (CSIC), 28006, Madrid, Spain



singly occupied orbital of OH with respect to the diatom rotation plane. The  $\Lambda$ -doublet pair of states is almost degenerate, but can be spectroscopically resolved due to different selection rules.

*Ab initio* calculations consistently predicted a collinear transition state<sup>7,17</sup> and a barrier height that increases as the reactants' approach moves away from collinear geometries. This effect is more pronounced on the  $^3A'$  PES, resulting in a steeper bending potential and consequently a narrower cone of acceptance. The steeper bending potential on the  $^3A'$  PES results in a higher vibrationally adiabatic potential (which includes the zero point energy) even though the electronic energy barrier is the same on the  $^3A'$  and  $^3A''$  PESs. At high collision energies,  $E_{\text{coll}}$ , the small difference in the adiabatic potentials is not relevant, but the narrower cone of acceptance leads to a lower reactivity on the  $^3A'$  PES. All the characteristics of the PESs allow us to conclude that the reactivity should always be lower on the  $^3A'$  PES than on the  $^3A''$  PES.

Although the symmetry of the  $\Lambda$ -doublet states is referred to the diatom rotation plane of the products, and the symmetry of the PESs refers to the three-atom plane, the analysis of the  $\Lambda$ -doublet relative populations provides information about the reactivity on the two PESs, which otherwise could not be extracted. By explicitly considering the reaction stereodynamics, we developed a method to calculate  $\Lambda$ -doublet populations from adiabatic Quantum Mechanics (QM) and quasiclassical trajectory (QCT) scattering calculations.<sup>16,36</sup> This method was applied to the simulation and interpretation of the experiments by Minton, McKendrick and coworkers,<sup>3,4</sup> who determined the  $OD(^2\Pi)$  state-to-state  $\Lambda$ -double population ratio for  $O(^3P) + D_2$  collisions using crossed molecular beams with hyperthermal atomic oxygen and detection by laser-induced fluorescence. They found a significantly higher population for the  $\Pi(A')$   $\Lambda$ -doublet state compared to  $\Pi(A'')$  regardless of  $E_{\text{coll}}$ , and final vibrational state. Our theoretical treatment showed that at hyperthermal energies, the propensity towards  $\Pi(A')$  was caused by an additional mechanism on the  $^3A''$  PES which leads to a significant  $^3A'' \rightarrow \Pi(A')$  population transfer.

Recently, we studied the  $O(^3P) + H_2$  reaction in a wide range of collision energies from 0.2 eV (well below the electronic energy barrier) to 1.7 eV. QM and QCT calculations were performed on the PESs of ref. 17, which accurately reproduce the degeneracy of the collinear saddle point. Surprisingly, our results showed that although the  $^3A''$  PES is generally more reactive than the  $^3A'$  PES, this is not the case for energies around the vibrationally adiabatic barrier, for which the  $^3A'$  PES is slightly more reactive (up to a 10%) when  $H_2$  was in its ground rotational state. The prevalence of the  $^3A'$  PES was found to have been caused by a reorientation effect, which diverts some of the incoming flux towards collinear approaches where the reactivity is higher. This effect is absent on the  $^3A''$  PES. At  $E_{\text{coll}}$  below or near the barrier, this effect competes with tunnelling, which is favoured on the  $^3A''$  PES due to its narrower vibrationally adiabatic barrier. However, in a range of energies close to the barrier, the reorientation effect on the  $^3A'$  PES overcomes tunnelling on the  $^3A''$  PES, and the cross section on the  $^3A'$  PES is higher than on the  $^3A''$  PES. In this article, we

study the reaction of  $O(^3P) + D_2$ . Our results show that the reorientation effect is magnified, which we attribute to a smaller contribution of tunnelling due to the higher reduced mass of  $D_2$  compared to  $H_2$ . We predict that the preference for the  $^3A'$  PES is more important for vibrationally excited  $D_2$  and this is even reflected as a sharp peak on the  $\Pi(A')$   $\Lambda$ -doublet populations.

The article is laid out as follows: in Section 2, QM and the QCT scattering calculations are briefly described, with particular emphasis on the calculation of  $\Lambda$ -doublet cross sections and quantum deflection functions; in Section 3, the results are presented and discussed. The last section contains the summary of this work and the conclusions.

## 2 Methodology

### 2.1 QM scattering calculations

Time-independent QM scattering calculations were carried out using the ABC code<sup>37</sup> on the  $^3A'$  and  $^3A''$  PESs, described in ref. 17. For the  $O(^3P) + D_2$  reaction, calculations were carried out between 0.37 eV and 2.0 eV total energy, including all partial waves to convergence. The propagation was carried out in 300 log-derivative steps up to a maximum hyperradius,  $\rho_{\text{max}} = 15a_0$ . The maximum value of helicity was  $\Omega_{\text{max}} = 30$ . Additional calculations were carried out to describe the behavior of  $O(^3P) + D_2$  ( $\nu = 1$ ) at low collision energies, below the adiabatic barrier. In these additional calculations,  $\Omega_{\text{max}} = 15$ , and  $\rho_{\text{max}}$  was set to  $60a_0$  (in 2500 log-derivative steps). For the  $O(^3P) + H_2$  ( $\nu = 1, j = 0$ ) reaction, QM calculations were also carried out in the 0.01–1.71 eV collision energy range, using propagation in 300 log-derivative steps up to a  $\rho_{\text{max}} = 15a_0$ . The maximum value of helicity was  $\Omega_{\text{max}} = 26$ . At the lowest collision energies,  $\rho_{\text{max}} = 20a_0$  and  $\Omega_{\text{max}} = 15$ .

In this work, we will assume that the two states  $^3A'$  and  $^3A''$ , which are adiabatically correlated with the reactants and products, are uncoupled. Our calculations do not include the intersystem crossing (ISC) to the singlet  $^1A'$  PES. In previous studies using QCT and surface hopping, it was found that for the  $O + H_2$  system, the singlet state crosses the two triplet states after the barrier on the products side. So even if some collisions sample the singlet PES, spin-orbit coupling has a relatively minor effect on the dynamics of the system at  $E_{\text{coll}}$  above 0.4 eV while at energies near the threshold, the effect is negligible.<sup>8,38</sup> Similar conclusions have been drawn in a QM non-adiabatic study.<sup>13</sup> As for the Renner-Teller coupling between the  $^3A'$  and  $^3A''$  PESs, neither is considered. It is expected that its effect would be more pronounced at high orbital angular momentum (impact parameters) values. Be that as it may, the fact that there is a very good agreement between experimental results and QM calculations seems to indicate that a description of the reaction in terms of the two separate triplet PESs can account for detailed aspects of this reaction.<sup>1,11</sup>

### 2.2 Quasiclassical trajectories

QCT trajectories were run using the procedure described in ref. 39 and 40. The excitation function was calculated by



running batches of  $10^7$  trajectories for each  $D_2$  rovibrational state considered in this work. For each initial state,  $E_{\text{coll}}$  was chosen randomly and uniformly between 0.45 (0.3 for  $\nu = 1$ ) and 1.75 eV.<sup>39</sup> The trajectories were started at an atom–diatom distance of 10 Å using an integration step of  $3 \times 10^{-17}$  s, which guarantees a total energy conservation better than one part in  $10^5$ . For each collision energy, the maximum impact parameter,  $b_{\text{max}}(E_{\text{coll}})$ , was previously determined by running a reduced number of trajectories at several energies. The absolute maximum value of the impact parameter in the whole range of collision energies was found to be 1.6 Å. The rovibrational energies of the OD diatom were calculated by semiclassical quantisation of action using the diatomic potential (which is the same on the two PESs), with their values fitted to Dunham expansions. The real  $\nu'$  and  $j'$  values were rounded to their nearest integer value. The procedure to assign the  $\Lambda$ -doublet state is detailed in Section 2.3.

To describe the behavior near the classical energy threshold, we also calculated trajectories at fixed collision energies. Additional batches of  $2 \times 10^5$ – $5 \times 10^5$  trajectories were run at 7 collision energies between  $E_{\text{coll}} = 0.5$  and 0.65 eV (0.3–0.45 eV for  $\nu = 1$ ) on each of the two  $^3A'$  and  $^3A''$  PESs.

### 2.3 Calculation of $\Lambda$ -doublet cross sections

The calculation of the  $\Lambda$ -doublet cross sections from adiabatic QM or QCT calculations is carried out using the procedure described in ref. 16 and 36. It assumes that the reaction takes place independently on each of the PES, so that the state-to-state  $\Lambda$ -doublet integral cross sections are given by:

$$\sigma_{\text{R}}[\Pi(A')] = W_{A'}\sigma_{\text{R}}(A') + (1 - W_{A''})\sigma_{\text{R}}(A'') \quad (1)$$

$$\sigma_{\text{R}}[\Pi(A'')] = (1 - W_{A'})\sigma_{\text{R}}(A') + W_{A''}\sigma_{\text{R}}(A''), \quad (2)$$

where  $\sigma_{\text{R}}(A')$  and  $\sigma_{\text{R}}(A'')$  are the integral cross sections on the  $^3A'$  and  $^3A''$  PES, respectively,  $\sigma_{\text{R}}[\Pi(A')]$  and  $\sigma_{\text{R}}[\Pi(A'')]$  are the respective  $\Lambda$ -doublet cross sections for  $\Pi(A')$  and  $\Pi(A'')$ , and  $W_{A'}$  and  $W_{A''}$  (in short  $W_{A'/A''}$ ) are the factors connecting the cross sections on the two PESs and the populations of the  $\Pi(A')$  and  $\Pi(A'')$   $\Lambda$ -doublet states, respectively. It should be noted that  $W_{A'/A''}$  have to be calculated for each rovibrational state. As can be inferred from eqn (1) and (2), in all cases, the conservation of the total flux implies that  $\sigma_{\text{R}}(A') + \sigma_{\text{R}}(A'') = \sigma_{\text{R}}[\Pi(A')] + \sigma_{\text{R}}[\Pi(A'')]$ .

In ref. 16, it was demonstrated that  $W_{A'/A''}$  can be calculated from the distribution of helicities,  $\Omega'$ , and the projection of  $\mathbf{j}'$  on the products' recoil direction,  $\mathbf{k}'$ , can be determined using the expression:

$$W_{A'/A''} = 1 - \frac{\langle \Omega'^2 \rangle_{A'/A''}}{j'(j'+1)} \approx 1 - \left[ \frac{2[a_0^{(2)}]_{A'/A''} + 1}{3} \right]^{1/2}, \quad (3)$$

rendering  $W_{A'}$  or  $W_{A''}$  when  $\langle \Omega'^2 \rangle$  is calculated on  $^3A'$  or  $^3A''$  PESs, respectively. In eqn (3),  $a_0^{(2)}$  is the polarization moment that represents the alignment of the products' angular momentum obtained in a reference frame with  $z$  along  $\mathbf{k}'$ . This reference frame is rotated by the scattering angle,  $\theta$ , with respect to the

frame where  $z$  is along  $\mathbf{k}$ . In the latter reference frame,  $a_0^{(2)}$  can be measured experimentally.<sup>41,42</sup>

According to eqn (3), reactive flux from the  $^3A'$  PES populates  $\Pi(A')$  states ( $^3A' \rightarrow \Pi(A')$ ), and reactive flux from the  $^3A''$  PES populates  $\Pi(A'')$  states ( $^3A'' \rightarrow \Pi(A'')$ ) if  $\mathbf{j}'$  is aligned perpendicular to  $\mathbf{k}'$ . Similarly,  $^3A' \rightarrow \Pi(A'')$  ( $^3A'' \rightarrow \Pi(A')$ ) when  $\mathbf{k}'$  and  $\mathbf{j}'$  are parallel to each other. Neglecting the interference between the respective wave functions on the two PESs, it is also possible to define the  $\Lambda$ -doublet differential cross section (DCS), which is related to the DCS calculated on each of the PESs as:

$$\frac{d\sigma[\Pi(A')]}{d\omega} = W_{A'}(\theta)\frac{d\sigma(A')}{d\omega} + (1 - W_{A''}(\theta))\frac{d\sigma(A'')}{d\omega} \quad (4)$$

$$\frac{d\sigma[\Pi(A'')]}{d\omega} = (1 - W_{A'}(\theta))\frac{d\sigma(A')}{d\omega} + W_{A''}(\theta)\frac{d\sigma(A'')}{d\omega}, \quad (5)$$

where  $W_{A'/A''}(\theta)$  depend on the scattering angle, and can be calculated from the product Polarization-Dependent Differential Cross Sections (PDDCS)  $S_0^{(2)}(\theta)$  as:

$$W_{A'/A''}(\theta) \approx 1 - \left[ \frac{2[S_0^{(2)}(\theta)]_{A'/A''} + 1}{3} \right]^{1/2} \quad (6)$$

which is analogous to eqn (3) with the sole difference that the PDDCSs are used instead of the  $a_0^{(2)}$ , which depends on the final state and the scattering angle.<sup>43</sup>

### 2.4 Generalized quantum deflection functions

To shed light into the concurrent reaction mechanisms, it is useful to calculate the Generalized Quantum Deflection Functions (GDFs or  $Q_r(\theta, J)$ ), which are defined as the joint quasi-probability density function of  $J$  and  $\theta$ . Analysis of the GDFs makes possible to plot a  $J$ – $\theta$  map in which the mechanisms (and their interference) can be seen in different regions of the map. The GDF is defined as:<sup>44,45</sup>

$$Q_r(\theta, J) = \frac{1}{2j+1} \sum_{\nu', j'} \sum_{\Omega'} \sum_{J_1=0}^{J_{\text{max}}} \sum_{J_2=0}^{J_{\text{max}}} \frac{(\delta_{J_1, \nu'} + \delta_{J_2, J})}{2} \times f_{\Omega'\Omega}^{J_1}(\theta) f_{\Omega'\Omega}^{J_2^*}(\theta). \quad (7)$$

where  $f_{\Omega'\Omega}^J$ , the  $J$ -dependent scattering amplitude, is defined as:

$$f_{\Omega'\Omega}^J(\theta) = \frac{1}{2ik_{\text{in}}} (2J+1) d_{\Omega'\Omega}^J(\theta) S_{\Omega'\Omega}^J \quad (8)$$

where  $d_{\Omega'\Omega}^J(\theta)$  is the Wigner reduced rotation matrix element,  $k_{\text{in}}$  is the reactant's relative wavenumber, and  $S_{\Omega'\Omega}^J$  is an element of the scattering matrix, in which the indices related to the initial and final rovibrational states are omitted for the sake of simplicity. Please note that the GDF defined in eqn (7) includes the sum over the final states of the products and it is not multiplied by  $\sin \theta$  to better appreciate scattering at  $0^\circ$  and  $180^\circ$ .

Unlike the DCS, the GDFs can take positive or negative values (which indicate destructive interference). The latter,



however, are expected to be important only if state-to-state GDFs are calculated, as they will be probably washed out by the incoherent sum over final rovibrational states.

By analogy, it is possible to calculate the  $\Lambda$ -doublet resolved GDF, as:

$$Q_r^{A' \rightarrow \Pi(A')}(\theta, J) = \frac{1}{2j+1} \sum_{v', j'} \sum_{\Omega'} \sum_{J_1=0}^{J_{\max}} \sum_{J_2=0}^{J_{\max}} \frac{(\delta_{J_1, J} + \delta_{J_2, J})}{2} \times f_{\Omega'}^{J_1}(\theta) f_{\Omega'}^{J_2*}(\theta) \left( 1 - \left[ \frac{\Omega'^2}{j'(j'+1)} \right]^{1/2} \right) \quad (9)$$

if the calculations are performed on the  ${}^3A'$  PES. The same equation holds for the  $Q_r^{A'' \rightarrow \Pi(A'')}$  if the  $J$ -dependent scattering amplitudes were obtained from calculations on the  ${}^3A''$  PES. Analogously,

$$Q_r^{A' \rightarrow \Pi(A'')}(\theta, J) = \frac{1}{2j+1} \sum_{v', j'} \sum_{\Omega'} \sum_{J_1=0}^{J_{\max}} \sum_{J_2=0}^{J_{\max}} \frac{(\delta_{J_1, J} + \delta_{J_2, J})}{2} \times f_{\Omega'}^{J_1}(\theta) f_{\Omega'}^{J_2*}(\theta) \left( \left[ \frac{\Omega'^2}{j'(j'+1)} \right]^{1/2} \right) \quad (10)$$

when  $J$ -dependent scattering amplitudes are obtained from calculations on the  ${}^3A'$  PES (and  $Q_r^{A'' \rightarrow \Pi(A')}$  if they are obtained from calculations on the  ${}^3A''$  PES.

### 3 Results and discussion

Panel (a) of Fig. 1 shows the QM excitation function,  $\sigma_R(E_{\text{coll}})$ , representing the reactive cross section as a function of  $E_{\text{coll}}$ , for the  $\text{O}({}^3\text{P}) + \text{D}_2$  ( $v=0, j=0$ ) reaction calculated on the two PESs. The respective excitation functions calculated using QCT (not shown here) are in good agreement except near the threshold as classical trajectories cannot reproduce tunnelling. The  $\sigma_R(E_{\text{coll}})$  rises monotonically with increasing  $E_{\text{coll}}$ , as it is expected for a direct reaction featuring an electronic barrier. This behavior was also observed for the  $\text{O}({}^3\text{P}) + \text{H}_2$  reaction.<sup>10,11,17,18</sup> In the inset, it could be seen how the present calculations include the deep-tunneling region, with cross sections as low as  $10^{-12} \text{ \AA}^2$ . At these low energies, the  ${}^3A''$  PES is more reactive, as expected due to its lower and slightly narrower vibrational adiabatic barrier. The  ${}^3A'$  PES is also significantly more reactive for  $E_{\text{coll}} > 0.9 \text{ eV}$ , a consequence of the broader cone-of-acceptance. The cross-sections resolved in the two  $\Lambda$ -doublet

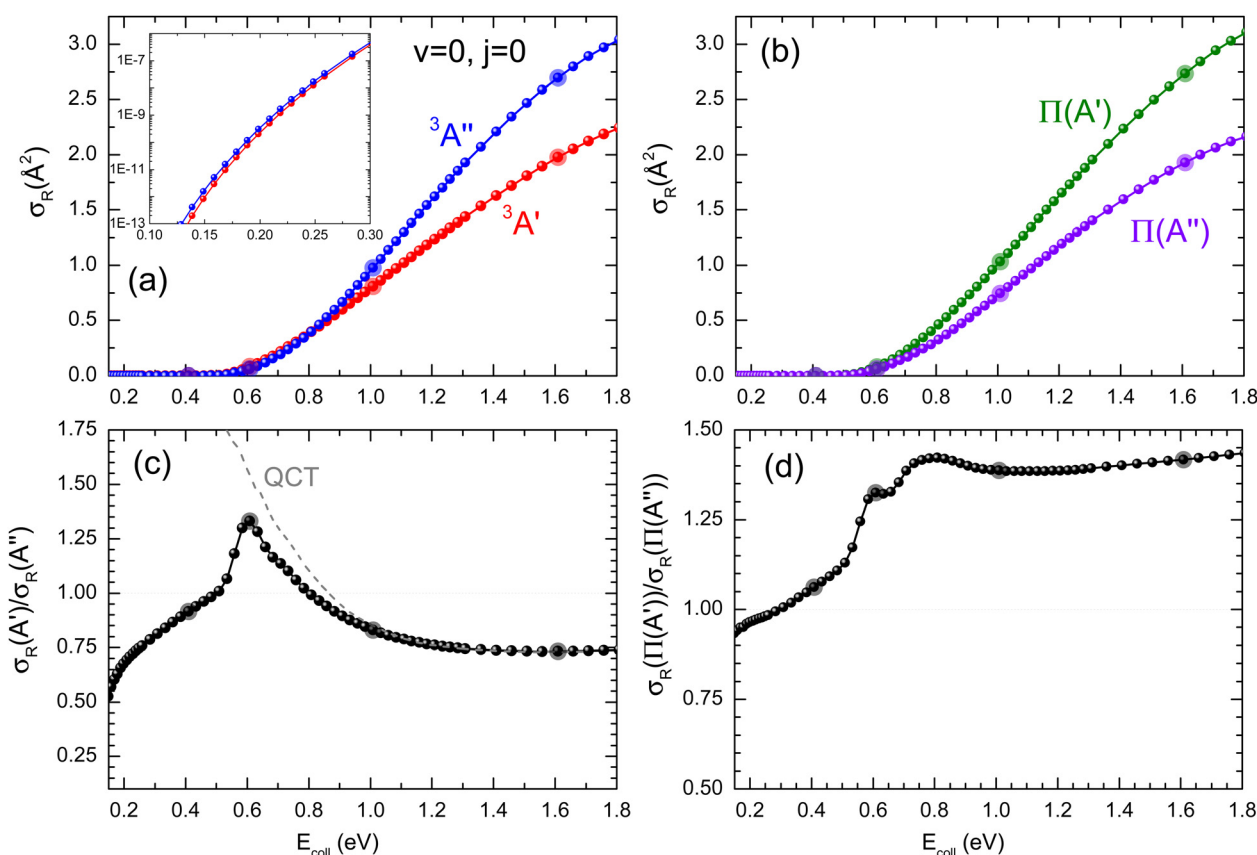


**Fig. 1** (a) QM excitation function summed over final states for the  $\text{O}({}^3\text{P}) + \text{D}_2$  ( $v=0, j=0$ ) reaction on the  ${}^3A'$  (red) and  ${}^3A''$  PES (blue). The inset represents the excitation function for low  $E_{\text{coll}}$  in the logarithm scale. (b) QM excitation function resolved in the two  $\Lambda$ -doublet manifolds:  $\Pi(A')$  (dark green) and  $\Pi(A'')$  (purple). (c) Ratio between the QM cross sections on the  ${}^3A'$  and  ${}^3A''$  PES as a function of  $E_{\text{coll}}$ . QCT results are shown as the dashed grey lines. (d) Ratio between the QM cross sections resolved in the two  $\Lambda$ -doublet manifolds. Results for  $E_{\text{coll}} = 0.41 \text{ eV}$ ,  $0.6 \text{ eV}$ ,  $1.0 \text{ eV}$ , and  $1.6 \text{ eV}$ , for which  $P(J)$  and DCS are shown in Fig. 2 and/or Fig. 3 and 4 are highlighted.



manifolds are shown in panel (b). As it was observed experimentally,<sup>3,4</sup> the  $\Pi(A')$  manifold is more populated, in contrast to what could be expected if  ${}^3A'' \rightarrow \Pi(A'')$ . The relative  $\sigma_R(E_{\text{coll}})$  values calculated as  $\sigma_R(A')/\sigma_R(A'')$  are shown in panel (c). As it was observed in the inset of panel (a), the  ${}^3A''$  PES is more reactive than the  ${}^3A'$  PES in the tunneling region, especially at the lowest energies where differences in the adiabatic barrier have a stronger effect on the dynamics. However, in the 0.5–0.8 eV  $E_{\text{coll}}$  range, around the classical barrier, the  ${}^3A'$  PES is up to 32% more reactive than the  ${}^3A''$  PES. For  $E_{\text{coll}} > 0.8$  eV, the  ${}^3A''$  PES is again more reactive, reaching the  $\sigma_R(A')/\sigma_R(A'')$  ratio a value of 0.75.

Based only on the shape of the PESs, it is not obvious why  ${}^3A'$  should be more reactive than  ${}^3A''$  in a particular range of  $E_{\text{coll}}$ . Moreover, the QCT results also predict that close to the classical threshold, the  ${}^3A'$  PES is significantly more reactive, ruling out the hypothesis that the higher  ${}^3A'$  reactivity is a consequence of a quantum effect such as a resonance. A similar effect was observed for the  $\text{O}({}^3\text{P}) + \text{H}_2$  reaction, although in this case,  $\sigma_R(A')$  was never more than 15% higher than  $\sigma_R(A'')$ .<sup>18</sup> Through the analysis of QCT trajectories for the  $\text{O}({}^3\text{P}) + \text{H}_2$  reaction, we found that the higher reactivity on the  ${}^3A'$  PES is a consequence of non-collinear trajectories, hitting the strong repulsive walls of the  ${}^3A'$  potential and being reoriented towards collinearity, for which the barrier is smaller and could lead to the reaction. Below the vibrationally adiabatic barrier, this effect competes with tunnelling, which is more important for the  ${}^3A''$  PES, so that the  ${}^3A'$  PES is only more reactive in the vicinity of the classical barrier, where the non-tunneling reaction is also possible. There is no tunneling in the QCT

calculations, so for energies just above the classical barrier, the reorientation pathway is the only possible option, explaining the higher reactivity on the  ${}^3A'$  PES. With increasing  $E_{\text{coll}}$ , the effect of the wider cone of acceptance of the  ${}^3A''$  PES dominates over the reorientation effect and the  ${}^3A''$  PES becomes more reactive again. The present results for  $\text{O}({}^3\text{P}) + \text{D}_2$  ( $v = 0, j = 0$ ) confirm this hypothesis. For  $\text{O}({}^3\text{P}) + \text{D}_2$ , the tunneling contribution, which favours the reactivity on the  ${}^3A''$  PES, is less important for  $\text{D}_2$  due to its larger reduced mass and to the broader adiabatic barrier. As a consequence, the reorientation effect will be more important for  $\text{D}_2$  than for  $\text{H}_2$ , leading to a higher relative reactivity of the  ${}^3A'$  state compared to the  ${}^3A''$  state, which can exceed 30% (compared to 15% in the case of  $\text{H}_2$ ). As we will see later, this effect has strong implications on the prevalence of  $\Pi(A')$  states for this isotopic variant. As shown in panel (d) of Fig. 1, the  $\Pi(A')$  manifold is more populated than the  $\Pi(A'')$  states for  $E_{\text{coll}} \geq 0.3$  eV.

To better understand the existence of an energy range in which the  ${}^3A'$  PES is more reactive, we show in Fig. 2 the QM total reaction probability as a function of the total angular momentum,  $P(J)$ , calculated at four  $E_{\text{coll}}$ ; namely, at 0.41 eV, well below the classical barrier and where the reactivity is mediated by tunnelling; at 0.6 eV, where  ${}^3A'$  is more reactive; and at 1.0 eV and 1.6 eV, where  ${}^3A''$  is again more reactive. For  $E_{\text{coll}} = 0.41$  eV,  $P(J)$  shows the typical shape of a direct reaction: it peaks at  $J = 0$  and decreases slowly with increasing  $J$  due to the effect of the centrifugal barrier. The reaction probability for the two PESs is very similar, with the  ${}^3A''$  being more reactive for all but the largest  $J$ s, where the value of the  $P(J)$  is negligible.

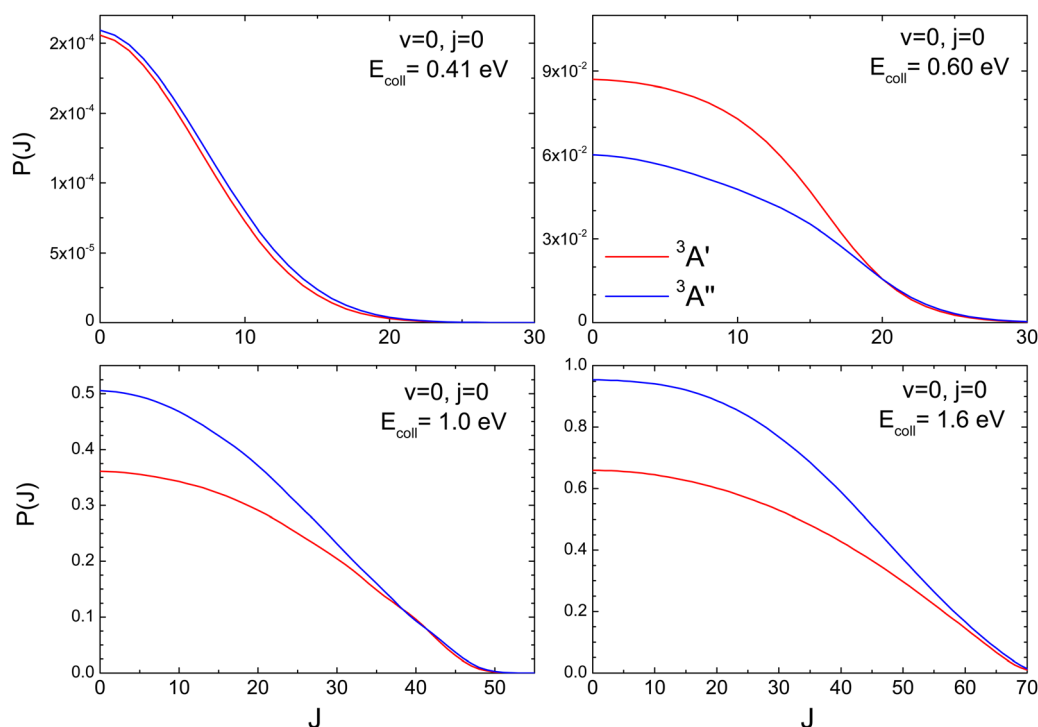


Fig. 2 Comparison of the QM total reaction probabilities as a function of the total angular momentum,  $P(J)$ , on the  ${}^3A'$  PES (red line) and  ${}^3A''$  PES (blue) for the  $\text{O}({}^3\text{P}) + \text{D}_2$  ( $v = 0, j = 0$ ) reaction calculated at four  $E_{\text{coll}}$ : 0.41 eV, 0.60 eV, 1.0 eV, and 1.6 eV.



At  $E_{\text{coll}} = 0.6$  eV, the shape of the  $P(j)$  is similar, showing a plateau for the lowest  $J$  and decreasing with increasing  $J$ . However, we observe a clear preference for the  $^3A'$  PES at low  $J$ s, while at high  $J$ , both  $P(j)$  converge. In fact, while the  $\sigma_{\text{R}}(A')/\sigma_{\text{R}}(A'')$  ratio reaches a maximum value of 1.32, the ratio of  $P(J=0; A')/P(J=0; A'')$  reaches a maximum value of 1.62. With increasing  $E_{\text{coll}}$  (to 1.0 and 1.6 eV), the shape of the  $P(j)$  does not change, and differences between  $^3A'$  and  $^3A''$  PESs are also more important at low  $J$ , although in this case the  $^3A'$  PES is more reactive. Regardless of the energy, we observe that the difference in reactivity between the two PESs cannot be attributed to the effect of the centrifugal barrier, which becomes more important at the highest  $J$ .

The DCSs resolved in the  $\Pi(A')$  and  $\Pi(A'')$   $\Lambda$ -doublet manifolds at  $E_{\text{coll}} = 0.6$  eV, 1.0 eV, and 1.6 eV are shown in Fig. 3, where we also show the DCS obtained only on the  $^3A'$  PES (middle panels) and on the  $^3A''$  PES (lower panels). Results for  $E_{\text{coll}} = 0.41$  eV are not shown because of their small value of the cross sections.

At 0.6 eV, the shape of the  $\Pi(A')$  and  $\Pi(A'')$  DCS is similar, both showing a clear preference for backward scattering. This behaviour at low energies suggests the existence of a direct

abstraction mechanism, similar to the so-called the *spiral* mechanism in ref. 46, where there is a correlation between low  $J$  and extreme backward angles.<sup>44</sup> At  $E_{\text{coll}} = 0.6$  eV, it is found that  $\sigma_{\text{R}}(\Pi(A'))$  is larger than  $\sigma_{\text{R}}(\Pi(A''))$ , and the DCS shows that this preponderance is due to the flux scattered at backward angles,  $\theta = 130$ – $180^\circ$ , where the  $\Pi(A')$   $\Lambda$ -doublet state is preferentially produced. In order to understand the origin of this preponderance, we have analyzed the flux leading to  $\Pi(A')$  and  $\Pi(A'')$  on the two PESs. We found that  $\Pi(A')$  OD states are preferentially populated on the  $^3A'$  PES, while a higher population is observed for the  $\Pi(A'')$  states on the  $^3A''$  PES. Furthermore, the conversion  $^3A' \rightarrow \Pi(A'')$  (the amount of flux from  $^3A'$  leading to  $\Pi(A'')$  OD states) is similar to  $^3A'' \rightarrow \Pi(A')$ . Thus the overall preference for the  $\Pi(A')$  is due to the higher reactivity on the  $^3A'$  PES, which is due to the reorientation effect.

At  $E_{\text{coll}} = 1.0$  eV, the  $\Pi(A')$  DCS is larger for  $\theta > 80^\circ$ , the region which accounts for most of the reactive flux. The analysis of the fluxes leading to  $\Pi(A')$  and  $\Pi(A'')$  on the two PESs shows that in this case, it is a consequence of a higher  $^3A'' \rightarrow \Pi(A')$  contribution, which is mainly responsible for scattering at sideways angles ( $\approx 100^\circ$ ). One might wonder whether the sideways bump in the DCS on the  $^3A''$  PES could

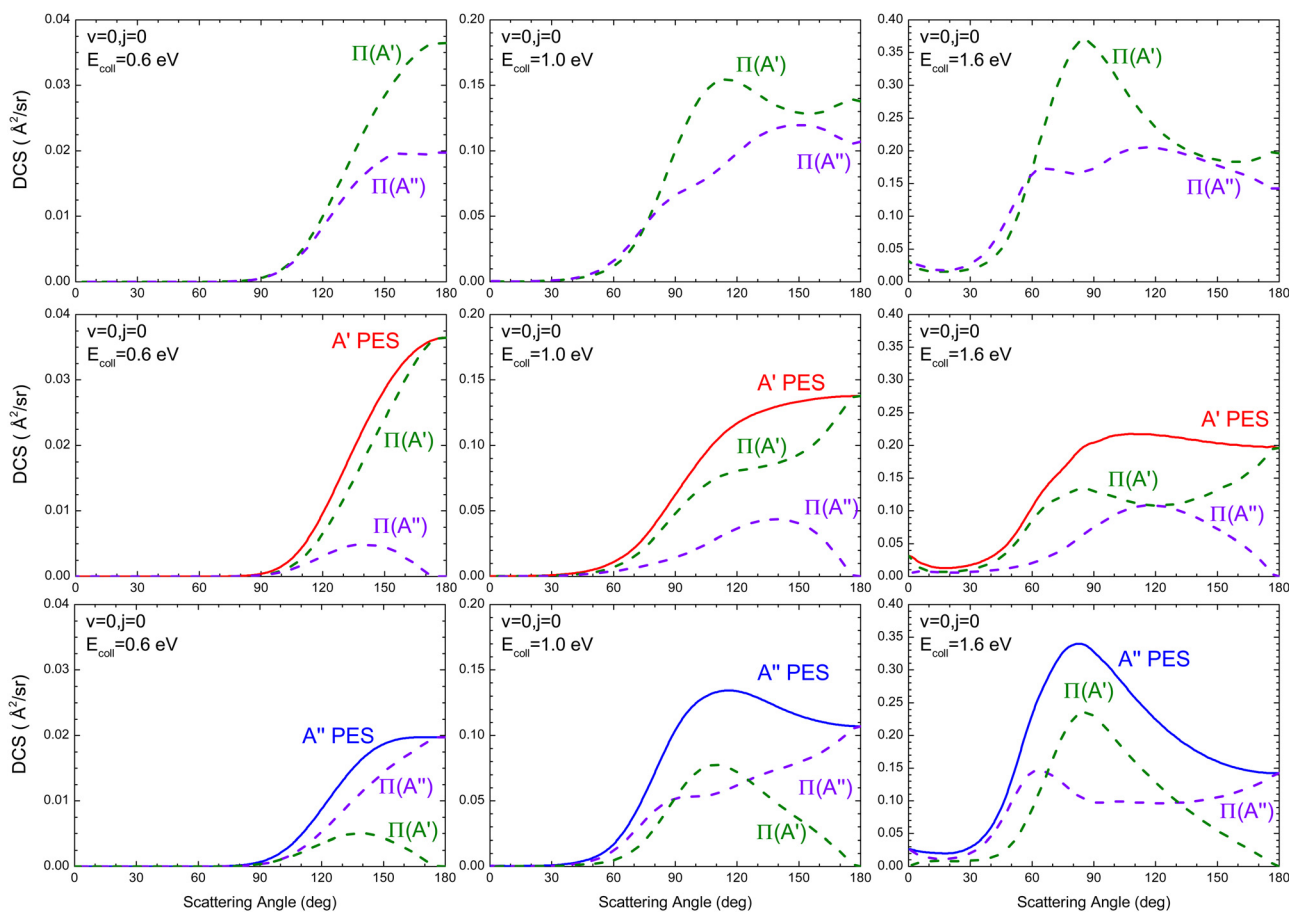


Fig. 3 Top panels: QM DCS summed over  $v'$  and  $j'$  states but resolved on the two  $\Lambda$ -doublet manifolds for the  $\text{O}(^3\text{P}) + \text{D}_2$  ( $v = 0, j = 0$ ) reaction at three  $E_{\text{coll}}$ : 0.6 eV, 1.0 eV, and 1.6 eV. Middle panels: QM DCS calculated only on the  $^3A'$ . The dashed lines represent the contributions from the  $^3A'$  PES to  $\Pi(A')$  and  $\Pi(A'')$ . Bottom panels: QM DCS calculated only on the  $^3A''$  PES showing its contributions to both  $\Lambda$ -doublets.



be caused by a higher contribution from higher  $J$ s. However,  $P(J)$  at high  $J$  is similar on both PESs, ruling out this possibility. With increasing energy,  $E_{\text{coll}} = 1.6$  eV, the shape of the  $\Pi(A')$  and  $\Pi(A'')$  is very different, with the former featuring a relatively sharp sideways peak, due to the  ${}^3A'' \rightarrow \Pi(A')$  contribution. This peak has the same origin as the bump observed at 1.0 eV, and it is not observed on the  ${}^3A'$  PES, not even at 1.6 eV. Outside the sideways region, the reactivity leading to  $\Pi(A')$  and  $\Pi(A'')$   $\Lambda$ -doublet states is similar. In ref. 16, we attributed the preference for  $\Pi(A')$  states at high  $E_{\text{coll}}$  to the existence of one additional mechanism on the  ${}^3A''$  PES that produces  $\Pi(A')$  states. The DCS calculated here confirms this hypothesis. It is another mechanism that ultimately causes that  $\Pi(A')$  to be more populated at high energies, as has been observed experimentally.

Regardless of the  $E_{\text{coll}}$  and the PES considered, most of the OD is originated in its vibrational ground state ( $v' = 0$ ). To gain more insight into the mechanisms, Fig. 4 shows the rotational distribution (cross section as a function of  $j'$ ) for  $v' = 0$  resolved in the  $\Lambda$ -doublet at the three energies for which the DCSs were also calculated. Independent of  $E_{\text{coll}}$ , the overall preference for  $\Pi(A')$  states is higher for medium to high values of  $j'$ , especially

at  $E_{\text{coll}} = 1.6$  eV. When we analyzed the population of the  $\Lambda$ -doublet states obtained from the  ${}^3A'$  PES, we found that the population of  $\Pi(A')$  states is always higher, especially for high  $j'$  values. Mechanistically, this means that  $j'$  is preferentially aligned perpendicular to  $\mathbf{k}'$ . On the  ${}^3A''$  PES, in turn, at  $E_{\text{coll}} = 0.6$  eV, the population on the  $\Pi(A'')$  is larger, but with increasing  $E_{\text{coll}}$ ,  $\Pi(A')$  dominates, especially for low  $j'$ . Mechanistically, this means that at low  $E_{\text{coll}}$ ,  $j'$  is preferentially aligned perpendicular to  $\mathbf{k}'$  (as on the  ${}^3A'$  PES), but with increasing  $E_{\text{coll}}$ ,  $j'$  is preferentially aligned along  $\mathbf{k}'$ , suggesting the existence of an additional mechanism on the  ${}^3A''$  PES at high  $E_{\text{coll}}$ .

In order to characterize this reaction mechanism, we have calculated the GDFs at 1.6 eV on the  ${}^3A'$  and  ${}^3A''$  PES, which are depicted in panels (a) and (b) of Fig. 5. On the  ${}^3A'$  PES, we observe a broad band diagonally across the  $\theta$ - $J$  map with a negative slope, which is similar to the mechanism in which low  $J$ s correlate with extreme backward angles (spiral).<sup>46</sup> The GDF on the  ${}^3A''$  PES shows two main bands: a broad one with a negative slope (as on the  ${}^3A'$  PES), which has a maximum at  $J = 45$  and  $\theta = 70^\circ$  and results in the sideways maximum observed on the DCS (Fig. 3), and a narrower band with a positive slope running from  $\theta = 120^\circ$  to  $180^\circ$  and  $J = 0$ -20.

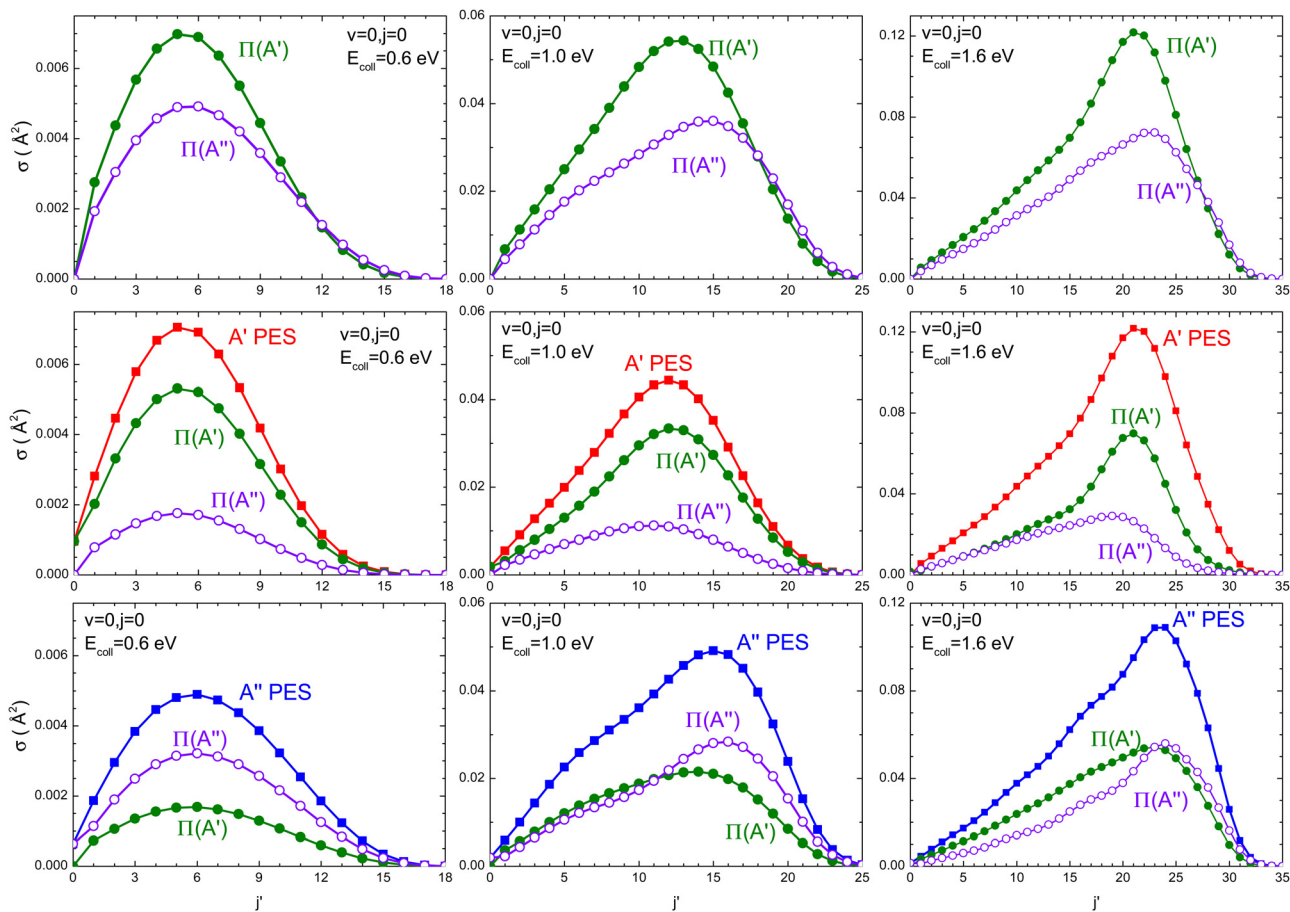


Fig. 4 Top panels: QM rotational distribution (cross section as a function of  $j'$ ) for  $v' = 0$  resolved on the two  $\Lambda$ -doublet manifolds for the  $O(^3P) + D_2$  ( $v = 0, j = 0$ ) reaction at three  $E_{\text{coll}}$ : 0.6 eV, 1.0 eV, and 1.6 eV. Middle panels: QM rotational distribution calculated only on the  ${}^3A'$  PES. Bottom panels: QM rotational distribution calculated only on the  ${}^3A''$  PES.



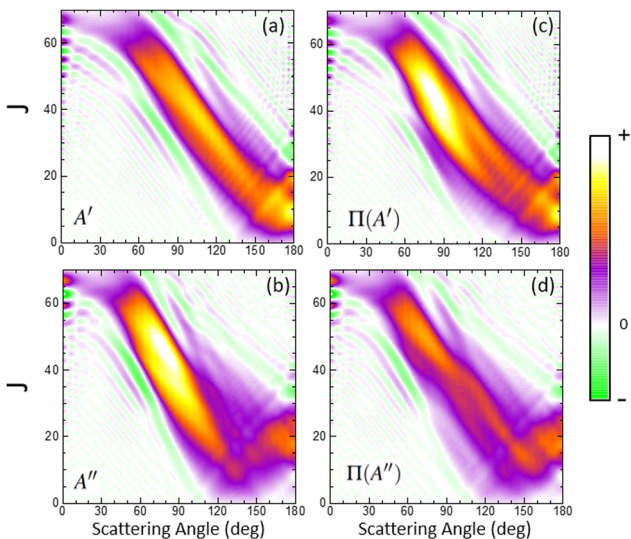


Fig. 5 Generalized quantum deflection functions (GDF) calculated on the  $^3A'$  PES, panel (a), and  $^3A''$ , panel (b), PES for the  $O(^3P) + D_2$  ( $v = 0, j = 0$ ) reaction at  $E_{\text{coll}} = 1.6$  eV. The GDFs resolved in the  $\Pi(A')$  and  $\Pi(A'')$   $\Lambda$ -doublet manifolds are shown in panels (c) and (d), respectively. The color scale is indicated in the figure, with the green contours corresponding to destructive interference ( $Q_r(\theta, J) < 0$ ).

Fig. 5 also shows the GDF corresponding to the reaction leading to the  $\Pi(A')$  (panel (c)) and  $\Pi(A'')$  (panel (d))  $\Lambda$ -doublet states. The shapes are similar to those on the  $^3A'$  and  $^3A''$  PES, although that of  $\Pi(A')$  is more intense in the sideways region at the expense of the  $\Pi(A'')$  GDF.

When the contribution from  $^3A'$  to  $\Pi(A')$  is singled out (see Fig. 6(a)), two regions where the GDF reaches a maximum value can be observed. The first, at  $\theta \approx 180^\circ$ , is identical to that

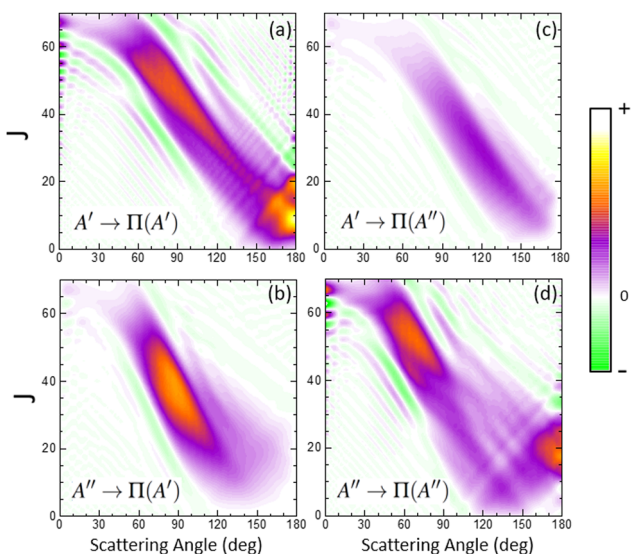


Fig. 6 Generalized quantum deflection functions (GDF) for the contribution of  $^3A'$  and  $^3A''$  PESs to  $\Pi(A')$  and  $\Pi(A'')$   $\Lambda$ -doublet states:  $^3A' \rightarrow \Pi(A')$ , panel (a),  $^3A'' \rightarrow \Pi(A')$ , panel (b),  $^3A' \rightarrow \Pi(A'')$ , panel (c), and  $^3A'' \rightarrow \Pi(A'')$ , panel (d). Color scale is indicated in the figure, with the green contours corresponding to destructive interference ( $Q_r(\theta, J) < 0$ ).

found on the  $^3A'$  PES, and the other at  $\theta \approx 70^\circ, J = 35 \pm 10$ . The GDF showing the  $^3A'' \rightarrow \Pi(A'')$  contribution (panel (c)) is rather faint, appearing as a background signal to the GDF observed on the  $^3A'$  PES. The GDF for the  $^3A' \rightarrow \Pi(A')$  contribution shows a single maximum at  $(\theta = 80^\circ, J = 20-55)$ , which includes most of the signal observed on the  $^3A''$  PES in this region. The  $^3A'' \rightarrow \Pi(A'')$  contribution to the GDF presents two maxima that are connected through a region with small values of the GDF. Mechanistically,  $^3A'' \rightarrow \Pi(A'')$  and  $^3A' \rightarrow \Pi(A')$  correspond to flux in which  $\mathbf{j}'$  is preferentially aligned perpendicular to  $\mathbf{k}'$ , while  $^3A'' \rightarrow \Pi(A')$  and  $^3A' \rightarrow \Pi(A'')$  mean that  $\mathbf{j}'$  is preferentially aligned along  $\mathbf{k}'$ . From our results, we conclude that the latter are responsible for the  $\Pi(A')$  preponderance, in particular the strong maximum for  $^3A'' \rightarrow \Pi(A')$ .

Overall, our results conclude that at high  $E_{\text{coll}}$ , the preference from  $\Pi(A')$  states comes from an additional mechanism on the  $^3A''$  PES, which occurs for moderate to high values of  $J$  ( $J \sim 35$  at  $E_{\text{coll}} = 1.6$  eV), where OD nascent molecules are scattered in the sideways region with their rotational angular momentum aligned perpendicular to the recoil direction.

In our previous calculations for  $O(^3P) + H_2$ , we observed that the  $H_2$  rotational excitation suppresses the reorientation effect, so that the  $^3A'$  PES is no more reactive than the  $^3A''$  PES, and the  $\sigma_R(A')/\sigma_R(A'')$  ratio did not show a maximum near the classical barrier.  $\sigma_R(A')/\sigma_R(A'')$  ratio calculations for  $O(^3P) + D_2$  ( $v = 0, j = 2$ ) (Fig. 7) show that while the ratio in QM calculations never exceeds one, a maximum can be observed at energies around the classical barrier, where the values of cross-sections on the  $^3A'$  and  $^3A''$  PES are very similar. Therefore, the suppression of the reorientation effect is not complete and, in fact, for the QCT calculation, the  $^3A'$  PES is slightly more reactive at energies just above the energy threshold. These differences are reflected in the propensity for  $\Pi(A')$  states, a phenomenon only observed for  $E_{\text{coll}} > 0.55$  eV. Outside the classical barrier region, the results are very similar to those for  $D_2$  ( $j = 0$ ), and  $^3A''$  is more reactive due to the broadening of the cone of acceptance.

As it was mentioned in the introduction, collisions between  $O(^3P)$  and vibrationally excited  $H_2$  play an important role in the formation of OH in the upper atmosphere or in the photon-dominated region of the interstellar space.<sup>21,27</sup> Accordingly, we have also studied the reaction of  $O(^3P) + D_2$  ( $v = 1, j = 0$ ). The results shown in Fig. 8 are similar to those obtained for  $D_2$  ( $v = 0, j = 0$ ), although all the features appear at lower  $E_{\text{coll}}$ , as a consequence of lowering of the adiabatic barriers with the vibrational excitation of the reactants. For  $v = 1$ , the maximum of the  $\sigma_R(A')/\sigma_R(A'')$  ratio is slightly higher than for  $v = 0$ , and our calculations show that this is also due to the higher reactivity on the  $^3A'$  PES at low  $J$  (results not shown). In fact, when only the  $J = 0$  partial wave is considered, the maximum value of the ratio is slightly above 1.8. The sharp maximum in the  $\sigma_R(A')/\sigma_R(A'')$  ratio is reflected in the  $\sigma(\Pi(A'))/\sigma(\Pi(A''))$  ratio, which also shows a peak at energies around the classical barrier.

Differences in the  $\sigma_R(A')/\sigma_R(A'')$  ratios for the different rovibrational states as well as for the two isotopic variants are shown in Fig. 9. While at high  $E_{\text{coll}}$ , the ratios converge to the





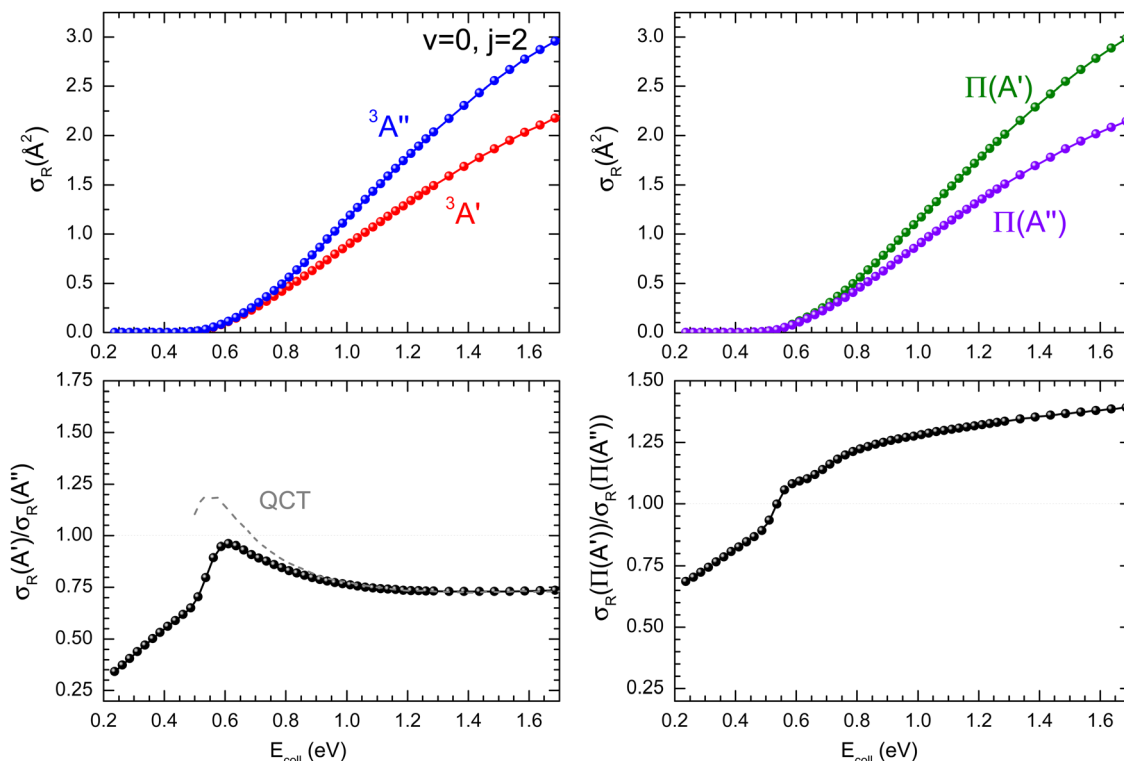


Fig. 7 Same as Fig. 1 but for the  $O(^3P) + D_2$  ( $v = 0, j = 2$ ) reaction.



Fig. 8 Same as Fig. 1 but for the  $O(^3P) + D_2$  ( $v = 1, j = 0$ ) reaction.

same value ( $\approx 0.75$ ), and the differences between the  $O(^3P) + H_2/D_2$  reactions are important close to their classical barrier.

First, the energy range in which  $^3A'$  is more reactive is broader for the reaction with  $D_2$ , which also shows a more positive



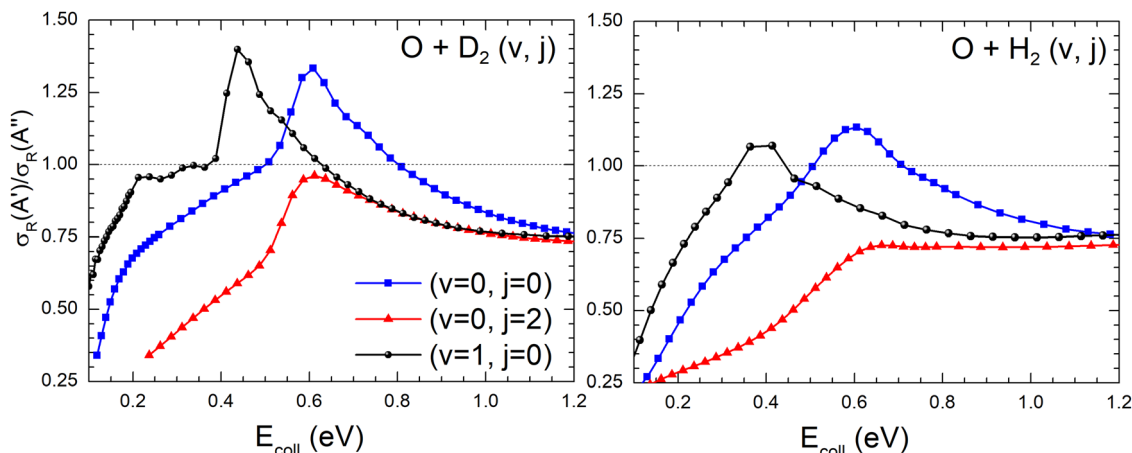


Fig. 9 Comparison of the ratios of the QM cross sections on the  $^3A'$  and  $^3A''$  PES as a function of  $E_{\text{coll}}$  for the  $O(^3P) + D_2(v,j)$  (left panel) and  $O(^3P) + H_2(v,j)$  reactions (right panel).

$\sigma_R(A')/\sigma_R(A'')$  ratio. This is a consequence of more efficient tunnelling in the collision with  $H_2$ , which partly compensates for the reorientation effect. Since for  $D_2$ , this contribution is smaller, the reorientation effect will be more pronounced. Second, while the rotational excitation suppresses the aforementioned maximum for collisions with  $H_2$ , this maximum is not completely washed out for  $D_2$  ( $j = 2$ ) although it is not sufficient to make the  $^3A'$  PES more reactive.

## 4 Conclusions

We have studied the dynamics of the  $O(^3P) + D_2$  reaction using time-independent QM scattering calculations over a wide range of collision energies, ranging from the deep tunnelling region, where the reactivity is very low, due to the high electronic barrier, to relatively high collision energies, where the collision energy is significantly higher than the electronic barrier and the cone of acceptance becomes wider. The reaction can take place on two potential energy surfaces (PESs) of symmetries  $^3A'$  and  $^3A''$ , both of which are degenerate at the saddle point. The former exhibits a higher and wider vibrationally adiabatic barrier due to the higher bending frequency at the transition state. Based on the shape of the PESs, one would expect that the  $^3A''$  PES, with a less stiff bending potential, should be more reactive at all energies. However, this is not the case at energies close to the classical barrier, where the  $^3A'$  PES becomes significantly more reactive (up to a 32%). We attribute the higher reactivity on the  $^3A'$  PES to a reorientation effect, which diverts incoming flux towards collinear approaches where the barrier is lower and hence the reactivity is higher. This effect competes with tunnelling across the vibrationally adiabatic barrier. Since tunnelling below the barrier is much lower for the  $O(^3P) + D_2$  reaction than for the  $O(^3P) + H_2$  reaction, the importance of the reorientation effect is higher for the former reaction. With increasing collision energy, both tunnelling and reorientation become less important, and the reactivity on the  $^3A''$  PES, with a wider cone of acceptance, is significantly higher than on the  $^3A'$  PES.

Our calculations show that for collision energies above the deep tunnelling region, the  $OD(^2\Pi)$  produced by the reaction preferentially populates the  $\Pi(A')$  manifold. This is a consequence of two effects: (i) at energies around the classical barrier, most of the reactivity on the  $^3A'$  ( $^3A''$ ) PES produces  $\Pi(A')$  ( $\Pi(A'')$ ) OD, so the higher reactivity on the  $^3A'$  PES leads to the higher  $\Pi(A')$  population; (ii) with the increasing collision energy, the  $^3A''$  PES becomes more reactive, but the presence of an additional mechanism on the  $^3A''$  PES leads to the higher population on the  $\Pi(A')$  states. Analysis of the generalized deflection function showed that this mechanism is associated with relatively high partial waves giving rise to sideways scattering. The rotational excitation of  $D_2$  partially suppresses the reorientation effect, ultimately leading to a preference for  $\Pi(A'')$  states at energies around the classical barrier. From relatively high collision energies, the QCT calculations of the ratio of the cross sections calculated on the  $^3A'$  and  $^3A''$  PESs are in good agreement with the results from QM calculations, suggesting that the new mechanism on the  $^3A''$  PES has a classical origin. At low collision energies, the QCT method fails to reproduce the QM ratio of the cross sections calculated on the  $^3A'$  and  $^3A''$  PESs and predicts higher reactivity on the  $^3A'$  PES. This is due to the absence of tunneling in classical trajectories, so that at very low collision energies, only the reorientation effect is important in QCT trajectories.

## Conflicts of interest

There are no conflicts to declare.

## Acknowledgements

The authors gratefully acknowledge grant PID2020-113147GA-I00, PID2021-122839NB-I00, PID2019-107115GB-C21 and PID2021-122549NB-C21 funded by Spanish Ministry of Science and Innovation (MCIN/AEI/10.13039/MCIN/AEI/10.13039/501100011033).



## Notes and references

- 1 D. J. Garton, T. K. Minton, B. Maiti, D. Troya and G. C. Schatz, *J. Chem. Phys.*, 2003, **118**, 1585–1588.
- 2 D. J. Garton, A. L. Brunsvold, T. K. Minton, D. Troya, B. Maiti and G. C. Schatz, *J. Phys. Chem. A*, 2006, **110**, 1327–1341.
- 3 S. A. Lahankar, J. Zhang, K. G. McKendrick and T. K. Minton, *Nat. Chem.*, 2013, **5**, 315.
- 4 S. A. Lahankar, J. Zhang, T. K. Minton and K. G. McKendrick, *J. Am. Chem. Soc.*, 2014, **136**, 12371–12384.
- 5 J. M. Bowman, *Chem. Phys. Lett.*, 1987, **141**, 545.
- 6 D. C. Chatfield, R. S. Friedman, G. C. Lynch, D. G. Truhlar and D. W. Schwenke, *J. Chem. Phys.*, 1993, **98**, 342.
- 7 D. Rogers, A. Kuppermann and S. Walsh, *J. Phys. Chem. A*, 2000, **104**, 2308.
- 8 M. R. Hoffmann and G. C. Schatz, *J. Chem. Phys.*, 2000, **113**, 9456.
- 9 J. Han, X. Chen and B. R. Weiner, *Chem. Phys. Lett.*, 2000, **332**, 243.
- 10 N. Balakrishnan, *J. Chem. Phys.*, 2003, **119**, 195–199.
- 11 N. Balakrishnan, *J. Chem. Phys.*, 2004, **121**, 6346–6352.
- 12 P. F. Weck, N. Balakrishnan, J. Brandao, C. Rosa and W. Wang, *J. Chem. Phys.*, 2006, **124**, 074308.
- 13 J. Zhao, *J. Chem. Phys.*, 2013, **138**, 134309.
- 14 J. Brandao, W. Wang and C. M. A. Rio, *Univ. J. Chem.*, 2015, **3**, 80.
- 15 P.-Y. Zhang and S.-J. Lv, *Commun. Comput. Chem.*, 2013, **1**, 63.
- 16 P. G. Jambrina, A. Zanchet, J. Aldegunde, M. Brouard and F. J. Aoiz, *Nat. Commun.*, 2016, **7**, 13439.
- 17 A. Zanchet, M. Menéndez, P. G. Jambrina and F. J. Aoiz, *J. Chem. Phys.*, 2019, **151**, 094307(1-10).
- 18 P. G. Jambrina, A. Zanchet, M. Menéndez, V. J. Herrero and F. J. Aoiz, *Phys. Chem. Chem. Phys.*, 2019, **21**, 25389–25396.
- 19 W. Tsang and R. F. Hampson, *J. Phys. Chem. Ref. Data*, 1986, **15**, 1087.
- 20 I. Glassman and R. A. Yetter, *Combustion*, Academic Press, 2008.
- 21 L. M. Reynard and D. J. Donaldson, *Geophys. Res. Lett.*, 2001, **28**, 2157.
- 22 M. M. Graff and A. Dalgarno, *Astrophys. J.*, 1987, **317**, 432.
- 23 M. Agúndez, J. Cernicharo and J. Goicoechea, *Astron. Astrophys.*, 2008, **483**, 831.
- 24 D. Fedele, S. Bruderer, E. F. van Dishoeck, J. Carr, G. J. Herczeg, C. Salyk, N. J. Evans, J. Bouwman, G. Meeus, T. Henning, J. Green, J. R. Najita and M. Güdel, *A & A*, 2013, **559**, A77.
- 25 B. Godard, E. Falgarone and G. Pineau des Forêts, *A & A*, 2014, **570**, A27.
- 26 J. R. Goicoechea, L. Chavarra, J. Cernicharo, D. A. Neufeld, R. Vavrek, E. A. Bergin, S. Cuadrado, P. Encrenaz, M. Etxaluze, G. J. Melnick and E. Polehampton, *ApJ*, 2015, **799**, 102.
- 27 A. Veselinova, M. Agúndez, J. R. Goicoechea, M. Menéndez, Z. Zanchet, E. Verdasco, P. G. Jambrina and F. J. Aoiz, *A & A*, 2021, **648**, A76.
- 28 M. Zannese, B. Tabone, E. Habart, J. R. Goicoechea, A. Zanchet, E. F. van Dishoeck, M. C. van Hemert, J. H. Black, A. G. G. M. Tielens, A. Veselinova, P. G. Jambrina, M. Menendez, E. Verdasco, F. J. Aoiz, L. Gonzalez-Sanchez, B. Trahin, E. Dartois, O. Berne, E. Peeters, J. He, A. Sidhu, R. Chown, I. Schroetter, D. V. D. Putte, A. Canin, F. Alarcon, A. Abergel, E. A. Bergin, J. Bernard-Salas, C. Boersma, E. Bron, J. Cami, D. Dicken, M. Elyajouri, A. Fuente, K. D. Gordon, L. Issa, C. Joblin, O. Kannavou, B. Khan, O. Lacinbala, D. Languignon, R. L. Gal, A. Maragkoudakis, R. Meshaka, Y. Okada, T. Onaka, S. Pasquini, M. W. Pound, M. Robberto, M. Rollig, B. Scheffer, T. Schirmer, S. Vicente and M. G. Wolfire, *Nat. Astron.*, 2024, DOI: [10.1038/s41550-024-02203-0](https://doi.org/10.1038/s41550-024-02203-0).
- 29 T. L. Nguyen and J. F. Stanton, *J. Phys. Chem. A*, 2014, **118**, 4918–4928.
- 30 A. A. Westenberg and N. de Haas, *J. Chem. Phys.*, 1967, **47**, 4241–4246.
- 31 P. Marshall and A. Fontijn, *J. Chem. Phys.*, 1987, **87**, 6988–6994.
- 32 J. V. Michael, *J. Chem. Phys.*, 1989, **90**, 189–198.
- 33 Y. F. Zhu, S. Arepalli and R. J. Gordon, *J. Chem. Phys.*, 1989, **90**, 183–188.
- 34 K. S. G. W. C. J. Yang and H. X. Shin, *Chem. Phys. Lett.*, 1993, **207**, 69–74.
- 35 M. H. Alexander, *Nat. Chem.*, 2013, **5**, 253–255.
- 36 P. G. Jambrina, M. Menéndez, A. Zanchet, E. García and F. J. Aoiz, *J. Phys. Chem. A*, 2018, **122**, 2739–2750.
- 37 D. Skouteris, J. F. Castillo and D. E. Manolopoulos, *Comput. Phys. Commun.*, 2000, **133**, 128–135.
- 38 B. Maiti and G. C. Schatz, *J. Chem. Phys.*, 2003, **119**, 12360.
- 39 F. J. Aoiz, L. Bañares and V. J. Herrero, *J. Chem. Soc., Faraday Trans.*, 1998, **94**, 2483–2500.
- 40 F. J. Aoiz, V. J. Herrero and V. Sáez-Rábanos, *J. Chem. Phys.*, 1992, **97**, 7423–7436.
- 41 T. R. Sharples, J. G. Leng, T. F. M. Luxford, K. G. McKendrick, P. G. Jambrina, F. J. Aoiz, D. W. Chandler and M. L. Costen, *Nat. Chem.*, 2018, **10**, 1148.
- 42 C. G. Heid, V. Walpole, M. Brouard, P. G. Jambrina and F. J. Aoiz, *Nat. Chem.*, 2019, **11**, 662–668.
- 43 J. Aldegunde, M. P. de Miranda, J. M. Haigh, B. K. Kendrick, V. Sáez-Rábanos and F. J. Aoiz, *J. Phys. Chem. A*, 2005, **109**, 6200–6217.
- 44 P. G. Jambrina, M. Menéndez and F. J. Aoiz, *Chem. Sci.*, 2018, **9**, 4837.
- 45 P. G. Jambrina, M. Menéndez, A. Zanchet, E. García and F. J. Aoiz, *Phys. Chem. Chem. Phys.*, 2019, **21**, 14012–14022.
- 46 S. J. Greaves, D. Murdock and E. Wrede, *J. Chem. Phys.*, 2008, **128**, 164307.

